Detecting an underground tunnel by applying joint traveltime and waveform inversion

Wenbin Jiang[1,3], Colin A. Zelt[2], and Jie Zhang[3]

[1]Nanjing University, School of Earth Sciences and Engineering, Nanjing, Jiangsu, China.

[2]Rice University, Department of Earth, Environmental & Planetary Sciences, Houston, Texas, USA.

[3]University of Science and Technology of China, Geophysical Research Institute, School of Earth and Space Sciences, Hefei, Anhui, China.

Corresponding author: Jie Zhang; Email: jzhang25@ustc.edu.cn

Email: wbjiang@nju.edu.cn

E-mail: czelt@rice.edu

Abstract

Underground tunnel and void detection is a challenging geophysical problem, and many methods have been proposed. Seismic techniques are promising because of the large seismic velocity contrasts between the air-filled void and the surrounding sediment and concrete. We apply a joint seismic traveltime and waveform inversion method to image a buried tunnel with concrete walls and a void space inside. The joint inversion images the top of the concrete tunnel as a high-velocity anomaly and the void space as a low-velocity anomaly. The location of the velocity anomalies predicted by the method agrees with the known location of the tunnel. As a comparison, the stand-alone full waveform inversion is also applied to the data. The first-arrival traveltime tomography shows weak nonlinearity but fails to image the hidden low-velocity layer. Full waveform inversion is able to image complex near-surface structures, but fitting waveforms may not honor the traveltime fit, especially when the data contain noise. Synthetic and real data tests show that the joint inversion method retains the advantages of both traveltime inversion and full waveform inversion and overcomes their respective drawbacks at the same time. The field example shows the joint inversion provides a better reconstruction of the high-velocity feature representing the top of the concrete wall in terms of its magnitude and location.

Keywords: Underground tunnel detection; Full waveform inversion; Joint inversion; Seismic data processing

1. Introduction

Over the past several decades, many geophysical methods have been proposed to detect underground tunnels and void spaces, such as electromagnetic (EM), gravity, ground-penetrating radar (GPR), and seismic refraction, diffraction, and surface-wave methods. These techniques are based on the large contrast in physical properties such as electrical resistivity, density, and seismic velocity between the air-filled cavity, the surrounding concrete, if any, and the host geologic medium (Butler, 1984; Belfer et al. 1998; Van Schoor, 2002; Mochales et al. 2008; Kaufmann et al. 2011; Sloan et al. 2015; Chen et al. 2017; Hauquin and Mourey, 2019; Lai et al. 2018; Alsharahi et al. 2019).

Butler (1984) detects a shallow air-filled cavity system and a deeper water-filled cavity system using a microgravity survey. The use of the vertical gravity gradient along the profile line helps detect shallow (less than 6 m) anomalous features. Mochales et al. (2008) present a combination of gravity, magnetic, and GPR surveys to detect underground cavities. These three methods are based on different physical properties. The sequential use of three methods allows the detection of cavities with different fill, such as air, water, and debris, that are difficult to resolve with only one or two approaches. Kaufmann (2011) applies gravimetry and electrical resistivity imaging to detect underground caves in the southern Harz mountains of Germany. The density of the air- and water-filled voids is much lower than the surrounding host rock. The water-filled cavity is more electrically conductive than the host rock, while the air-filled cavity is less conductive. Hauquin and Mourey (2019) apply 2D electrical resistivity tomography technique to detect masonry tunnels above subsurface cavities. The tunnels are imaged as low resistivity anomalies because of a highly resistive layer (caused by moisture and seepage water deposits) around it. Hong Kong highways department carry out a blind test to evaluate the feasibility of GPR method in underground void detection (Lai et al. 2018). An acceptance criterion is designed according to the international standard and local experience. Results provided by six local service companies are not satisfactory, which indicates the difficulty of void detection in the urban area. Kilic and Eren (2018) conduct a GPR survey to obtain an image of voids and karst conduits. Furthermore, a three-layer neural network is applied in the detection process.

All the above nonseismic methods have advantages and limitations in detecting embedded anomalies. Gravity and GPR methods are effective in identifying shallow cavities. However, gravity data are insensitive to the void if it is buried deeper than the size of the void (Wightman et al., 2003). The GPR method depends on the contrast in the dielectric properties between the target and host overburden. The penetration depth of the GPR signal is limited in lossy sediments (Slob et al. 2010; Luo et al. 2019), and the void cannot be detected if it is filled with water. The EM approach provides no useful information on the material below high electrically conductive areas. Moreover, the EM approach requires longer electrode arrays in the case of deeper voids, which makes the detection difficult (Wightman et al., 2003). Therefore, the potential-field methods are usually applied in regions where the target is large and shallow. Compared with the gravity, GPR and EM approaches, seismic methods are more reliable for detecting smaller objects because of better resolution and penetration under various conditions.

Belfer et al. (1998) apply refraction tomography to detect short-wavelength velocity variations. Furthermore, a diffraction stack is used to delineate local scattering objects. Seismic diffractions result from a subsurface discontinuity that acts as a secondary radiation source and produces hyperbolic events in seismic records. Backscattered surface waves are caused by surface waves that scatter back toward the source when reaching a lateral interface. Conventional seismic data processing workflows seek to enhance reflected energy while suppressing diffractions and surface waves because both are considered to be noise in reflection imaging. Xia et al. (2007) demonstrate that the Raleigh-wave diffractions in the shot gather can be used to detect 2D void and fault. However, a sophisticated data preprocessing is required to preserve weak diffracted surface waves. Sloan et al. (2015) apply P-wave diffraction and surface-wave backscatter approaches to detect a subterranean tunnel. Compared with reflections, the amplitude of the diffractions is weak. The backscattered surface waves are mixed with the forward propagating surface-wave energy. A sophisticated preprocessing workflow needs to be applied to the seismic data to extract diffractions and backscattered surface-wave energy. Tran et al. (2013) apply 2D time-domain full waveform inversion to detect an air-filled sinkhole. Both body waves and Rayleigh waves are used to invert P- and S-wave velocities. Chen et al. (2017) demonstrate the capability of using frequency-dependent traveltime tomography (FDTT) and frequency-domain full waveform inversion (FWI) to detect a known target tunnel. The embedded air-filled void space is imaged as a low-velocity anomaly. The workflow of applying FDTT followed by FWI shows the capability of detecting subwavelength-scale features. Chen et al. (2017) present frequency-domain FWI of P and SH waves. In the present study, joint inversion is implemented in the time-domain with an acoustic approximation, and only P-wave data are inverted.

Ray-based first-arrival traveltime tomography has been widely applied for estimating near-surface velocity (Zhu et al. 1992; Zhang and Toksöz, 1998; Leung and Qian, 2006; Park and Pyun, 2018). However, traveltime inversion usually produces a suboptimal estimate of subsurface velocity because it assumes an infinite frequency approximation of the data, although Zelt and Chen (2016) present a frequency-dependent traveltime inversion methodology. FWI is a robust tool for imaging near-surface structures, which improves the velocity estimation with higher resolution (Tarantola, 1984; Pratt et al. 1998; Wang et al. 2019). A fundamental challenge of FWI is to avoid a local minimum in the model space caused by the nonlinearity of the inverse problem. FWI requires a good starting model to avoid cycle-skipping between the synthetic and observed data (Virieux and Operto, 2009). Researchers have made significant efforts to develop new FWI algorithms and strategies that can avoid or mitigate the cycle-skipping problem. Zhang and Chen (2014) propose a joint first-arrival traveltime and waveform inversion method to estimate near-surface velocities. The method minimizes the misfit function for both traveltimes and waveform simultaneously, which helps mitigate the nonlinearity of the inversion. Jiang and Zhang (2015) apply the joint traveltime and waveform inversion method to image complex near-surface structures in the Yumen oil field. Fan et al. (2015) demonstrate the effectiveness of the joint inversion method using real data from the North Sea.

The goal of this study is to detect a buried tunnel surrounded by concrete walls and filled with air. The burial depth of the anomalies is shallow and the geologic structure in the survey area is quite simple. We apply seismic methods to detect the embedded anomalies, specifically, we apply joint traveltime and waveform inversion to detect the underground tunnel and void space. We demonstrate the synthetic test results with two starting models: 1D linear gradient velocity model and traveltime tomography model. As a comparison, stand-alone FWI results are also presented using these two workflows. We also present real data results from FWI and the joint inversion.

In the following sections, we shall introduce the basic theory of joint inversion. Then, we present a synthetic test that is designed according to the prior knowledge of the target. Finally, we test the joint inversion method on real data acquired on the Rice University campus and previously analyzed using frequency-domain FWI by Chen et al. (2017).

2. Method

In this section, we review the basic theory of the joint inversion method. The joint inversion minimizes the traveltime and waveform residuals simultaneously by solving a nonlinear inverse problem. We refer readers to Zhang and Chen (2014) for more details.

In the time domain, the 2D acoustic-wave equation can be expressed as

$$\begin{aligned} -\frac{1}{\kappa}\frac{\partial \mathbf{P}}{\partial t} &= \nabla \cdot \mathbf{v} + \mathbf{S}, \\ \rho \frac{\partial \mathbf{v}}{\partial t} &= -\nabla \mathbf{P}. \end{aligned} \tag{1}$$

where $\mathbf{P}$ is pressure, $\mathbf{v}$ denotes particle velocity, κ and ρ are the bulk modulus and density, respectively, and $\mathbf{S}$ represents the source time function. The synthetic seismograms are generated by a staggered-grid finite-difference method with fourth-order accuracy in space and second-order accuracy in time (Zhang and Zhang, 2011). The free-surface boundary condition is applied on the top of the model, and the perfectly matched layer (PML) boundary conditions are used at the other three boundaries (Zhang and Shen, 2010). The traveltimes are calculated by wavefront raytracing (Zhang and Toksöz, 1998).

The objective function of the joint inversion is:

$$\Phi(\mathbf{m}) = (1-\omega)\left\|\mathbf{P}_{obs} - \mathbf{P}_{syn}(\mathbf{m})\right\|^2 + \omega\left\|\mathbf{t}_{obs} - \mathbf{t}_{syn}(\mathbf{m})\right\|^2 + \tau\left\|\mathbf{L}(\mathbf{m}-\mathbf{m}_0)\right\|^2,$$

(2)

where $\mathbf{P}_{obs}$ and $\mathbf{P}_{syn}$ represent the observed data and synthetic waveform, respectively. $\mathbf{t}_{obs}$ and $\mathbf{t}_{syn}$ are the picked first-arrival traveltimes and the synthetic traveltimes. $\mathbf{m}$ is the velocity model, and $\mathbf{m}_0$ is a prior model for the joint inversion. $\mathbf{L}$ denotes a Laplacian operator for regularization, and ω is a weighting factor between the waveform and traveltime misfits. τ is the regularization parameter. The joint inversion gradient is the summation of the weighted traveltime and waveform gradients. An optimal step length is calculated at each iteration to minimize the joint inversion misfit. The nonlinear optimization problem is solved by the conjugate gradient method. Only P wave velocities are inverted during the inversion. The density model is converted from P-wave velocity model according to Gardner's law (Gardner et al., 1974) in each iteration. And the converted density model is used in the forward modeling of synthetic waveforms.

Selection of weighting factor ω is an important issue in the joint inversion. We design an adaptive weighting factor selection strategy in this study. A large traveltime weighting factor is used at the beginning of the inversion process. The weighting factor gradually decreases as the inversion iterates. We run the joint inversion in the beginning to constrain the shallow velocities, and end up with waveform inversion to reconstruct the details. To be specific, we smoothly decrease the traveltime weighting factor from 0.8 to 0.2 during the inversion. The decreasing rate depends on the iteration number. The regularization parameter is fixed as 0.1 during the whole inversion process. The starting model is used as prior model $\mathbf{m}_0$ in the synthetic and field examples.

The first-arrival traveltimes and the early arrival waveforms represent different attributes of the seismic data. The infinite frequency traveltime tomography is based on ray theory, that can reconstruct macro-velocity structure. The waveform inversion takes the frequency content of the data into account. Therefore, it is more sensitive to small-scale heterogeneities. Furthermore, FWI resolves low-velocity anomalies better than traveltime tomography because first-arrival ray coverage is poor in low-velocity zone. The joint inversion method minimizes the misfit function for both traveltimes and waveforms in the inversion process. In this way, the joint inversion method can fit both data by combining different physical imaging theories (Zhang and Chen, 2014).

3. Numerical example

We apply the joint inversion method to data from a synthetic model. The true model is shown in Fig. 1a, which is designed according to the known information of the tunnel structure on the campus of Rice University (Chen et al. 2017). The velocity model is discretized with 240×100 cells, with a square cell size of 0.1 m. The tunnel is surrounded with concrete walls that are 0.6 m thick on the top and 0.3 m thick on the bottom and two sides. The void space within the tunnel is filled with air. The velocity of the concrete is 4000 m/s, and the air velocity is 340 m/s. In this study, we are dealing with a void surrounded by concrete. Therefore, there are two large velocity contrasts: between sediment and concrete, and between concrete and air. The background velocity increase from 200 m/s at the surface to 1000 m/s at the bottom. A 1D linear gradient initial model (Fig. 1b) is based on the true model. No prior information of the tunnel walls and the voids are included in the starting model.

To test the spatial resolving power and reliability of the survey geometry, we use the same shot and receiver intervals in the synthetic test as in the real data survey. The seismic geometry is perpendicular to the buried tunnel. The seismic survey line is 24 m long and includes 25 shots with an interval of 1 m and 72 receivers for each shot with an interval of 0.333 m. A 50 Hz peak frequency Ricker wavelet is used as the source wavelet in the finite-difference forward modeling. The first-arrival traveltimes are generated with wavefront raytracing (Zhang and Toksöz, 1998). Uncorrelated Gaussian-distributed random noise with a standard deviation of 5% is added to the traveltimes. The noise is proportional to the absolute traveltime, the standard deviation is approximately 4 ms for the longest offset (24 m).

We perform forward modeling tests to explore how the tunnel structure affects the waveform. Figure 2 shows the synthetic traveltime and waveform generated with the 1D linear-gradient background model and the true model. We observe an advance of the traveltime and early arrival waveform because of the high-velocity concrete tunnel walls (indicated by the black arrows).

The 1D linear-gradient model is used as the starting model for conventional ray-theory infinite-frequency traveltime tomography (Zhang and Toksöz, 1998). The traveltime misfit decreases to the same level as the reciprocal errors. The traveltime tomography model images the top of the high-velocity concrete wall at the correct position (Fig. 1c). However, traveltime tomography fails to image the low-velocity void space below the high-velocity top of the tunnel. FWI utilizes full wavefield information to improve the resolution of the geophysical properties estimation. The 1D background velocity model is used as a starting model for FWI and the joint inversion. The starting density model is converted from initial P wave velocity model according to Gardner's law, and it does not include the void and concrete. Both the FWI and joint inversion image the low-velocity anomaly associated with the void space. The joint inversion result appears to image the high-velocity anomaly associated with the concrete top wall more accurately than FWI (Figs. 3(a)–(b)). This is because the model gradient from traveltime helps reconstruct the velocity at the top of the concrete wall in the joint inversion. However, the high-velocity anomaly at the top of the concrete in the joint inversion result is much weaker than the one in the traveltime tomography result (Fig. 1c). The comparison between the observed and synthetic waveform data is presented in Fig. 4 for shot 9. The waveform match between observed and synthetic waveforms is excellent, but the traveltimes calculated with FWI and joint inversion model do not fit the observed traveltimes. The results suggest that a 1D laterally homogeneous velocity model is insufficient for this test using FWI and joint inversion. This inspires us to use the traveltime tomography result as an initial model for FWI and the joint inversion.

Figures 3(c)-(d) show the FWI and joint inversion results using the traveltime tomography result as the starting model. Compared with the traveltime tomography model, the position of the high-velocity tunnel is more accurate. The top concrete wall is centered at the correct lateral and vertical position. The joint inversion method reconstructs the tunnel features better than the FWI model with a stronger magnitude. Figure 5 shows the waveform overlay for shot 9. For the FWI, the waveform match is excellent but we still observe large traveltime differences between traveltimes calculated with the FWI result and observed traveltimes (Fig. 5b). Compared with FWI, the joint inversion improves matches of waveform and traveltime (Fig. 5c). The differences between the observed traveltimes and the synthetic traveltimes in figure 5b are partially caused by the random noise in the observed traveltimes. But we can also observe that the synthetic traveltimes are earlier than the observed traveltimes in the near-offset area (< 6 m), and larger than the observed traveltimes in the far-offset area (> 6 m). It is not randomly distributed, suggests that the traveltime differences are mainly caused by velocity error instead of noise. The excellent traveltime and waveform match suggests that the traveltime tomography result as a starting model is sufficient for joint inversion. The synthetic experiments verify the possibility of the workflow to image the tunnel in the real data application because the source-receiver geometry and the data frequency band are the same.

Figure 6 shows 1D velocity profiles through the middle of the tunnel to illustrate the performance of the inversion methods. The joint inversion models are superior to the comparable FWI models because they better reconstruct the high-velocity top concrete wall. In this case, the traveltime tomography model is comparable with the FWI model and joint inversion model in recovering the high-velocity top concrete wall. However, the FWI and joint inversion models better reconstruct the low-velocity void space. In addition, the velocity profiles show that the traveltime tomography model is a better starting model than the 1D linear gradient model.

Figure 7a shows the normalized waveform misfit curves of FWI and the joint inversion using the 1D starting model. The waveform misfit curves depict that the joint inversion misfit is slightly larger than the FWI misfit. Figure 7b is the traveltime misfit curve of the joint inversion. The traveltime misfit decreases from 3.6 ms to 0.9 ms. This clearly demonstrates that the joint inversion fits the traveltimes and waveforms simultaneously in the inversion process. Figure 8 shows the normalized waveform misfit and traveltime misfit using the traveltime tomography starting model. The waveform data misfits of the two methods decrease to about the same level. The traveltime misfit of the joint inversion increases at first because the traveltime tomography result served as the starting model. The traveltime misfit starts to decrease after four iterations. The final traveltime misfit is slightly larger than the initial value, but still acceptable given the data uncertainties.

Traveltime tomography followed by the joint inversion successfully detects the high-velocity top concrete wall and low-velocity air-filled void. However, FWI and joint inversion fail to image the two sides and the bottom concrete walls. There are several reasons for this. First, the central frequency of the data is about 50 Hz, the wavelength varies from 5-10 m in this case, which is too large compared with the 0.3 m thick concrete walls. Second, the first-arrival wave paths are focused along the top high-velocity concrete wall and are not sensitive to the sides and bottom of the tunnel underneath the top concrete wall. Therefore, the two sides and bottom concrete walls are below the resolution of FWI and the joint inversion.

4. Real data example

A seismic experiment to image a known concrete tunnel with air-filled void space was carried out on Rice University campus, Houston, Texas, USA, in 2011 (Chen et al. 2017). Data were collected on a grass field. The total length of the survey line is 24 m. The orientation of the tunnel is perpendicular to the survey line. The geometry includes 25 shots and 72 receivers, for a total of 1800 traces. The seismic data were collected by stacking ten hammer blows on a trailer hitch ball vertically mounted on the ground. A two-component version of a Galperin geophone was used for each receiver such that stacking the two components retains the vertical ground velocity and cancels out the horizontal motion (Chen et al. 2017). Figure 9 shows a raw shot gather collected at X=24 m and the corresponding average amplitude spectrum. Similar to the synthetic data, we can observe a traveltime and waveform advance due to the high-velocity concrete walls of the tunnel (indicated by the black boxes).

In this study, we use the first-arrival traveltimes picked by Chen et al. (2017). They used a semi-automated picking scheme and manually corrected a few picks. The average reciprocal error for all the shots is about 1 ms (Fig. 10), it is acceptable given the sampling rate and frequency band of 0.2 ms and 10-60 Hz, respectively. We obtained a best-fit 1D linear gradient velocity model using the Zelt and Smith (1992) algorithm. The 1D model serves as the starting model for 2D traveltime tomography (Jiang and Zhang, 2017). Figure 11a shows the traveltime tomography result. The high-velocity concrete top wall is imaged. The low-velocity anomaly below the top concrete wall is not nicely reconstructed due to the low illumination in this area.

The preprocessing of the waveform data is a crucial part of the workflow for FWI and the joint inversion of the field data. The primary objectives of the data processing are to improve the signal-to-noise ratio and to transform the field data such that they reflect the approximations made in the acoustic forward modeling. Therefore, it is necessary to preprocess the observed data to remove the seismic noise and elastic effects. Otherwise, the seismic noise and non-acoustic wavefield will be projected into the reconstructed P-wave velocity models. We apply a preprocessing workflow to the field data to preserve early-arrival waveforms. The early-arrival waveform data mainly includes refractions and diving waves, which are useful to build an accurate shallow velocity model. In this study, the field data are bandpass filtered with a 5-10-60-120 Hz bandwidth. The filtering aims to remove the low frequencies with a poor signal-to-noise ratio and to limit the maximum frequency content of the data to mitigate the cycle skipping problem. The dominant frequency of the early arrival waveform is about 50 Hz. We mute the seismic data before the picked first-arrival times to remove noise. A time window with a 10 ms cosine taper is applied to the data to exclude the surface waves and converted S-waves. During the inversion process, the near-offset data (< 4 m) are muted due to the strong surface wave present in the near-offset traces. Figure 9 shows the shot gather at X=24 m after preprocessing, including the windowing of the data and the associated amplitude spectrum.

Since FWI and joint inversion are performed in 2D, the source is modeled as a line source. While a hammer blow is a point source, the 3D effects may limit the capability of detecting underground tunnel and voids. As shown in Forbriger et al. (2014), a hybrid transformation to the point-source data is equivalent to line-source response. The simplest way to correct the phase is to convolve the waveforms with $\sqrt{t^{-1}}$, which corresponds to a phase shift of π/4. In this study, we have applied the amplitude correction to the observed data. We did not correct the phase of the observed data because applying a time shift to synthetic waveform is equivalent to a phase correction on narrow-band observed data. For a single frequency data, a phase shift of π/4 corresponds to a time shift of T/8 (T is the period of the data). The field data are bandpass filtered, and the dominant frequency of the early arrival waveform is about 50 Hz. Applying a phase shift of π/4 on narrow-band data is approximately equal to a time shift on synthetic waveform. However, we should mention that the method is not applicable to the broadband seismic data.

The wavelet extraction is tricky in the real data inversion. The source wavelet can be extracted through deconvolution when the minimum phase or zero phase of the source wavelet is true (Yilmaz, 2001).

While the source wavelet is mixed phase in the real case. The source wavelet inversion is linear under the assumption that the current velocity model is correct, which can be inverted during the first iteration in the frequency domain FWI (Pratt, 1999). Another approach is to invert the source wavelet and velocity model simultaneously in FWI. For the data with simple near-surface structures, the source wavelet can be extracted by stacking the near-offset first arrivals along the first breaks. However, the near-offset data are contaminated with high amplitude surface waves, extract source wavelet from near-offset first arrivals is difficult. Since the effective early arrival waveform are bandpass filtered to a specific bandwidth, a Ricker wavelet with a central frequency of 50 Hz is acceptable in this study.

The traveltime tomography result (Fig. 11a) is used as the starting model for FWI and the joint inversion to avoid cycle skipping and converging to a solution that represents a local minimum. The FWI and joint inversion models contain more small-scale structure than in the traveltime tomography model, and the position of the high-velocity top concrete wall is more accurate (Figs. 11(b)-(c)). To compare the performance of the methods in terms of how well they reconstruct the high-velocity top of the concrete tunnel and the low-velocity air below, we plot the 1D velocity-depth profiles (Fig. 12). The FWI and joint inversion models clearly image the low-velocity inside the tunnel better than the traveltime model, and they both image the top of the tunnel better in terms of location.

The input waveform data and synthetic data from the traveltime model are shown in Fig. 13a for a shot at X=24 m. The waveform advances (Fig. 9b) that are interpreted due to the high-velocity top of the concrete tunnel, are matched well by the traveltime tomography model predicted data. The far-offset waveforms (-24 to -18 m) show some mismatches, suggesting that the initial model needs to be updated to fit the observed data. Figures 13(b)-(c) show the final waveform overlay from FWI and the joint inversion. The far-offset data are significantly better matched by the FWI and joint inversion predicted data. A low-velocity anomaly is presented in the FWI and joint inversion to compensate the phase advances of the far-offset data. The matches of the first positive peak become worse. This is because the amplitude of the latter waveform is stronger, which dominates the waveform match in the inversion. We observe large traveltime difference between traveltimes calculated with the FWI result and picked traveltimes in far offset (Fig. 13b). The joint inversion matched traveltimes better than the waveform inversion (Fig. 13c). It suggests that FWI improves the waveform match but does not take traveltime into account. While the joint inversion fits both traveltime and waveform. In this study, we focus on the traveltime and early waveform advances (indicated by the black boxes in Fig. 9) due to the tunnel walls. Although we apply a mute function to exclude near-offset traces and later arrivals. Note that there are still some seismic events (surface waves, converted S-waves) that cannot be modeled by acoustic modeling, and were regarded as P-waves in the inversion. Since the arrival times of P-waves are earlier than surface waves and S-waves, these events might distort the deeper part of the inversion result, which is beneath the target area. An elastic full waveform inversion of recorded data is required in the future to quantitative analyze the influence of surface waves on the inversion result. Figure 14 shows the normalized waveform misfit and traveltime misfit of the FWI and joint inversion. The waveform data misfit of the joint inversion is slightly larger than FWI. Similar to the joint inversion traveltime misfit curve in the synthetic test, the traveltime misfit increases at first because the traveltime tomography result served as the starting model. The traveltime misfit starts to decrease after few iterations. The final traveltime misfit is also slightly larger than the initial value.

Comparisons of the FWI and joint inversion models show that the joint inversion model has a higher magnitude for the high-velocity feature representing the top of the concrete wall. The traveltime advances (Fig. 13c) which are interpreted to be due to the high-velocity top of the concrete tunnel, are significantly better matched by the joint inversion model's predicted traveltime data. FWI images the low-velocity inside the tunnel slightly better than the joint inversion. There are two reasons for this. First, the joint inversion fits the traveltimes at the far-offsets (21-24 m) better than FWI (Figs. 13b and 13c), and it thereby favors higher velocities in the void space. Second, the joint inversion traveltime gradient contains the high-velocity concrete wall feature, which would affect the low-velocity anomaly below due to the smoothing regularization.

As a comparison, the frequency domain FWI result that uses the FDTT model as the starting model (FDTT-FWI) in Chen et al. (2017) paper is also presented (Fig. 11d). The 1D velocity-depth profiles show that FDTT-FWI model presents the low-velocity feature representing the void space with a smaller value than in our FWI and joint inversion model. *e.g*, the minimum velocity is approximately 230 m/s in the FDTT-FWI model, while it is approximately 380 m/s in our FWI model. On the other hand, Our FWI and joint inversion models better reconstruct the tunnel features than the FDTT-FWI model with a stronger magnitude, *e.g*, a maximum of approximately 950 m/s for the top of the concrete tunnel in the FDTT-FWI model compared with a maximum of approximately 1250 m/s in the joint inversion model (Fig. 12). There are several possible reasons for the differences. First, the FDTT model contains a low-velocity anomaly below the top of the concrete corresponding to the void space, while our infinite frequency traveltime tomography model does not contain the low-velocity feature. The starting model would affect the final inversion result. Second, the smoothing strategies are different. No regularization was used in FDTT-FWI, but a low-pass wavenumber filter was applied to smooth the gradient. However, we apply Tikhonov regularization to stabilize the inversion. Finally, the difference between the frequency-domain and time-domain FWI code could also lead to the model difference.

5. Discussion

The air-filled void space is interpreted as a low-velocity zone in the acoustic FWI and joint inversion tests. A certain amount of waves will be trapped into the low-velocity zone, while 100% of the incident waves are scattered back at the air-solid interface in the real case. Since there are some differences between the air-filled void space and the low-velocity zone, we conduct several forward modeling tests to figure out whether the void space can be replaced by a low-velocity zone. The best replacement velocity is obtained by evaluating the waveform difference. The benchmark model contains an air-filled hole (Fig. 15a), which is the same size as the void space in the field data experiment. We then replace the air-filled hole with velocity anomalies ranging from 200 m/s to 480 m/s. The velocity interval is 10 m/s. Compared with the benchmark model, the differences are the surface topography and velocities in the anomaly area. We evaluate the differences of the waveform fit for the forward modeling results from these models and benchmark model. Figure 16 shows the normalized waveform difference with different replacement velocity. Forward modeling results show that a replacement velocity of 350 m/s yields the smallest waveform difference. Figure 15b compares the waveform between the benchmark model and model with 350 m/s replacement velocity. The overall waveform matches well except the strong near offset reflections from the left side of the air-filled hole and late arrivals in the far offset. The near offset seismic traces and late arrivals are usually muted in the early arrival waveform inversion of real data. Therefore, the inverted velocity models image the air-filled void space of the tunnel as a low-velocity anomaly.

6. Conclusions

In this study, we demonstrate the application of FWI and joint inversion to detect a known target. The size of the target anomalies is less than the dominant seismic wavelength. First-arrival traveltime tomography provides a better starting model for FWI and the joint inversion than a 1D linear velocity gradient model. FWI and the joint inversion use waveform information to improve the resolution to detect subwavelength scales. Both FWI and the joint inversion reconstruct the high-velocity top concrete wall and low-velocity void space inside the tunnel. The joint inversion images the top of the tunnel with better magnitude and spatial extent than the FWI, while FWI better reconstructs the low-velocity anomaly corresponding to the void space in the tunnel. The fit of the traveltime data in the joint inversion improves detection of the high-velocity concrete wall but degrades the image of the void space below, for reasons described previously. The workflow of applying traveltime tomography followed by the joint inversion shows the ability to detect near-surface subwavelength features. Compared with the FDTT-FWI result of Chen et al. (2017), our FWI and joint inversion models better recover the high-velocity tunnel features but produce a poorer low-velocity feature representing the void space in terms of magnitude, probably because of a better starting model for FWI provided by FDTT.

The extremely strong velocity variation and subwavelength dimensions of the target, make the goal of the study to be detection instead of imaging. Therefore, the magnitude of the anomalies is inaccurate, but it represents a success from the standpoint of detection.

Acknowledgments

We thank the editor and reviewers for their constructive comments and suggestions, which helped to improve the paper. We thank the financial support from National Natural Science Foundation of China (Grant No: 41674120) and the China Postdoctoral Science Foundation (Grant No: 2019M661791). The IRIS PASSCAL Instrument Center provided the seismic acquisition instruments. The acquisition of the real data and previous analysis by Chen et al. (2017) was funded by National Science Foundation grant EAR-1056073 and Department of Energy grant DE-FG07-97ER14827. We thank the volunteers in the Rice Earth, Environmental & Planetary Sciences Department for their help in acquiring the data. Wenbin Jiang thanks Rice University for making it possible for him to serve as a visiting student for one year. We thank Jianxiong Chen for providing his picks and model (Fig. 11d). We appreciate the support from GeoTomo, allowing us to use the TomoPlus software package to conduct the research.

References

Alsharahi, G., Faize, A., Louzazni, M., Mostapha, A.M.M., Bayjja, M., Driouach, A., 2019. Detection of cavities and fragile areas by numerical methods and GPR application. Journal of Applied Geophysics. 164, 225–236.

Belfer, I., Bruner, I., Keydar, S., Kravtsov, A., Landa, E., 1998. Detection of shallow objects using refracted and diffracted seismic waves. Journal of Applied Geophysics. 38, 155–168. https://doi.org/10.1016/s0926-9851(97)00025-6.

Butler, D.K., 1984. Microgravimetric and gravity gradient techniques for detection of subsurface cavities. Geophysics. 49, 1084–1096. https://doi.org/10.1190/1.1441723.

Chen, J.X., Zelt, C.A., Jaiswal, P., 2017. Detecting a known near-surface target through application of frequency-dependent traveltime tomography and full-waveform inversion to P-and SH-wave seismic refraction data. Geophysics. 82, R1-R17. https://doi.org/10.1190/geo2016-0085.1.

Fan, H., Bell, L., Deng, Y.L., Zhang, J., 2015. Imaging shallow complex structures in North Sea with joint traveltime and waveform inversion. *in* 2015 Workshop: Depth Model Building: Full-waveform Inversion, Beijing, China, Society of Exploration Geophysicists. 40-43. https://doi.org/10.1190/fwi2015-010.

Forbriger, T., Groos, L., Schäfer, M., 2014. Line-source simulation for shallow-seismic data. Part 1: Theoretical background: Geophysical Journal International, 198(3), 1387-1404.

Gardner, G.H.F., Gardner, L.W., Gregory A.R., 1974. Formation velocity and density - the diagnostic basics for stratigraphic traps: Geophysics, 39(8), 770–780.

Hauquin, T., Mourey, Q., 2019. The detection of old masonry tunnels as low electrical resistivity anomalies-application to one covered stream tunnel of the Cevennes Mountain region (France).

Journal of Applied Geophysics. 168, 12-23. https://doi.org/10.1016/j.jappgeo.2019.05.010.

Jiang, W., Zhang, J., 2015. Imaging complex near-surface land area with joint traveltime and waveform inversion. *in* Expanded Abstracts: 85^{th} Annual International Meeting, Society of Exploration Geophysicists. 1441-1445. https://doi.org/10.1190/segam2015-5863831.1.

Jiang, W., Zhang, J., 2017. First-arrival traveltime tomography with modified total-variation regularization. Geophysical prospecting. 65(5), 1138-1154.

Kaufmann, G., Romanov, D., Nielbock, R., 2011. Cave detection using multiple geophysical methods: Unicorn cave, Harz Mountains, Germany. Geophysics. 76(3), B71–B77. https://doi.org/10.1190/1.3560245.

Kilic, G., Eren, L., 2018. Neural network based inspection of voids and karst conduits in hydro–electric power station tunnels using GPR. Journal of Applied Geophysics. 151, 194-204. https://doi.org/10.1016/j.jappgeo.2018.02.026

Lai, W.W., Chang, R.K., Sham, J.F., 2018. A blind test of nondestructive underground void detection by ground penetrating radar (GPR). Journal of Applied Geophysics. 149, 10-17. https://doi.org/10.1016/j.jappgeo.2017.12.010

Leung, S., Qian, J., 2006. An adjoint state method for three-dimensional transmission traveltime tomography using first-arrivals. Communications in Mathematical Sciences. 4, 249-266. https://doi.org/10.4310/cms.2006.v4.n1.a10.

Luo, T.X.H., Lai, W.W..L., Chang, R.K.W., Goodman, D., 2019. GPR imaging criteria. Journal of Applied Geophysics. 165, 37–48. http://dx.doi.org/10.1016/j.jappgeo.2019.04.008.

Mochales, T., Casas, A.M., Pueyo, E.L., Pueyo, O., Roman, M.T., Pocovi, A., Soriano, M.A., Anson, D., 2008. Detection of underground cavities by combining gravity, magnetic and ground penetrating radar surveys: A case study from the Zaragoza area, NE Spain. Environmental Geology. 53, 1067–1077. https://doi.org/10.1007/s00254-007-0733-7.

Park, Y., Pyun, S., 2018. Refraction traveltime tomography based on damped wave equation for irregular topographic model. Journal of Applied Geophysics. 150, 160-171. https://doi.org/10.1016/j.jappgeo.2018.01.025.

Pratt, R. G., 1999. Seismic waveform inversion in the frequency domain. Part 1: Theory and verification in a physical scale model. Geophysics. 64, 888–901.

Pratt, R.G., Shin, C., Hicks, G.J., 1998. Gauss-Newton and Full Newton Methods in Frequency-space Seismic Waveform Inversion. Geophysical Journal International. 133, 341–362. https://doi.org/10.1046/j.1365-246x.1998.00498.x.

Sloan, S.D., Peterie, S.L., Miller, R.D., Ivanov, J., Schwenk, J.T., McKenna, J.R., 2015. Detecting clandestine tunnels using near-surface seismic techniques. Geophysics. 80(5), EN127–EN135. https://doi.org/10.1190/geo2014-0529.1.

Slob, E., Sato, M., Olhoeft, G., 2010. Surface and borehole ground-penetrating-radar developments. Geophysics. 75, 75A103–75A120. https://doi.org/10.1190/1.3480619.

Tarantola, A., 1984. Inversion of Seismic-reflection Data in the Acoustic Approximation. Geophysics. 49, 1259-1266. https://doi.org/10.1190/1.1441754.

Tran, K.T., McVay, M., Faraone, M., Horhota, D., 2013. Sinkhole detection using 2D full seismic waveform tomography. Geophysics. 78(5), R175-R183. https://doi.org/10.1190/geo2013-0063.1.

Van Schoor, M., 2002. Detection of sinkholes using 2D electrical resistivity imaging. Journal of Applied Geophysics. 50, 393–399. https://doi.org/10.1016/s0926-9851(02)00166-0.

Virieux, J., Operto, S., 2009. An Overview of Full-waveform Inversion in Exploration Geophysics. Geophysics. 74, WCC1–WCC26. https://doi.org/10.1190/1.3238367.

Wang, Z.Y., Huang, J.P., Liu, D.J., Li, Z.C., Yong, P., Yang, Z.J., 2019. 3D variable-grid full-waveform inversion on GPU. Petroleum Science. 16(5), 1001-1014.

Wightman, W., Jalinoos, F., Sirles, P., Hanna, K., 2003. Applications of geophysical methods to related highway problems: FHWA Technical manual.

Xia, J., Nyquist, J.E., Xu, Y., Roth, M.J., Miller, R.D., 2007. Feasibility of detecting near-surface feature with Rayleigh-wave diffraction. Journal of Applied Geophysics. 62(3), 244-253. https://doi.org/10.1016/j.jappgeo.2006.12.002.

Yilmaz, O., 2001, Seismic data analysis: Processing, inversion, and interpretation of seismic data: SEG.

Zelt, C.A., Chen, J., 2016. Frequency-dependent traveltime tomography for near-surface seismic refraction data. Geophysical Journal International. 207, 72–88. https://doi.org/10.1093/gji/ggw269

Zelt, C.A., Smith, R.B., 1992. Seismic traveltime inversion for 2-D crustal velocity structure. Geophysical journal international. 108, 16-34. https://doi.org/10.1111/j.1365-246x.1992.tb00836.x

Zhang, J., Chen, J., 2014. Joint Seismic Traveltime and Waveform Inversion for Near Surface Imaging. *in* Expanded Abstracts: 84th Annual International Meeting, Society of Exploration Geophysicists. 934-937. https://doi.org/10.1190/segam2014-1501.1.

Zhang, J., Toksöz, M.N., 1998. Nonlinear refraction traveltime tomography. Geophysics. 63, 1726–1737. https://doi.org/10.1190/1.1826562.

Zhang, W., Zhang, J., 2011. Full-waveform tomography with consideration for large topography variations. *in* Expanded Abstracts: 81^{st} Annual International Meeting, Society of Exploration Geophysicists. 2539–2542. https://doi.org/10.1190/1.3627719.

Zhang, W., Shen, Y., 2010. Unsplit complex frequency-shifted PML implementation using auxiliary differential equations for seismic wave modeling. Geophysics. 75(4), T141-T154. https://doi.org/10.1190/1.3463431.

Zhu, X., Sixta, D.P., Angstman, B.G., 1992. Tomostatics: turning-ray tomography+static corrections. The Leading Edge. 11(12), 15–23. https://doi.org/10.1190/1.1821921.

Figure captions

Fig. 1. (a) True model. (b) 1D linear gradient starting model. (c) Traveltime tomography models from synthetic data. The known concrete walls of the tunnel are indicated by black line.

Fig. 2. Synthetic traveltime and waveform data. The blue dots and red waveforms represent traveltime and waveform calculated with true model. The green dots and black waveforms denote traveltime and waveform calculated with 1D linear gradient model. Near-offset waveform data are muted. The traveltime and waveform advances due to the tunnel walls are indicated by the black arrows. (a) Shot gather for X=0 m, (b) X=9 m, and (c) X=13 m.

Fig. 3. FWI and the joint inversion models from synthetic data. (a) FWI model that uses the 1D model as the starting model. (b) The joint inversion model that uses the 1D model as the starting model. (c) FWI model that uses the traveltime tomography model as the starting model. (d) The joint inversion model that uses the traveltime tomography model as the starting model.

Fig. 4. Waveform overlay for shot gather at X=9 m using the 1D model as the starting model. (a) Initial waveform overlay. (b) FWI final waveform overlay. (c) Joint inversion final waveform overlay. Balck waveforms are observed data and red waveforms represent synthetic data. Blue dots denote observed traveltimes, green dots represent synthetic traveltimes.

Fig. 5. Waveform overlay for shot gather at X=9 m using the traveltime tomography model as the starting model. (a) Initial waveform overlay. (b) FWI final waveform overlay. (c) Joint inversion final

waveform overlay. Balck waveforms are observed data and red waveforms represent synthetic data. Blue dots denote observed traveltimes, green dots represent synthetic traveltimes.

Fig. 6. 1D velocity profiles as labeled at X=8 m in the middle of the tunnel.

Fig. 7. Data misfit of the synthetic tests using a 1D starting model. (a) Normalized waveform misfit of FWI and the joint inversion. (b) Traveltime misfit of the joint inversion.

Fig. 8. Data misfit of the synthetic tests using the traveltime tomography model as the starting model. (a) Normalized waveform misfit of FWI and the joint inversion. (b) Traveltime misfit of the joint inversion.

Fig. 9. (a) The raw shot gather of the real data at X=24 m. (b) The shot gather after preprocessing. (c) The average amplitude spectrum of the raw shot gather. (d) The average amplitude spectrum of the shot gather after preprocessing. Blue dots represent picked traveltimes. The waveform advances due to the tunnel walls are indicated by the black boxes.

Fig. 10. The reciprocal error of the shots. The average reciprocal error is about 1 ms.

Fig. 11. Final models from real data. (a) Traveltime tomography model that uses the 1D model as the starting model. (b) FWI model that uses the traveltime tomography model as the starting model. (c)

The joint inversion model that uses the traveltime tomography model as the starting model. (d) The frequency domain FWI result from Chen et al. (2017).

Fig. 12. 1D velocity profiles as labeled at X=8 m in the middle of the tunnel.

Fig. 13. Waveform overlays of a shot gather at X=24 m. (a) Waveform overlay between observed data (black) and synthetics (red) associated with traveltime tomography result. (b) Waveform overlay between observed data (black) and synthetics (red) associated with FWI result. (c) Waveform overlay between observed data (black) and synthetics (red) associated with the joint inversion result. Blue dots denote picked traveltimes, green dots represent synthetic traveltimes.

Fig. 14. Data misfit of the real data test (a) Normalized waveform misfit of FWI and the joint inversion. (b) Traveltime misfit of the joint inversion.

Fig. 15. (a) Benchmark model with an air-filled hole. The red star denotes shot, yellow triangles represent receivers. The red line is the surface topography. (b) Waveform overlay of the shot gather from Benchmark model (black) and model with 350 m/s replacement velocity (red).

Fig. 16. Normalized waveform difference between velocity models filled with replacement velocity and benchmark model.

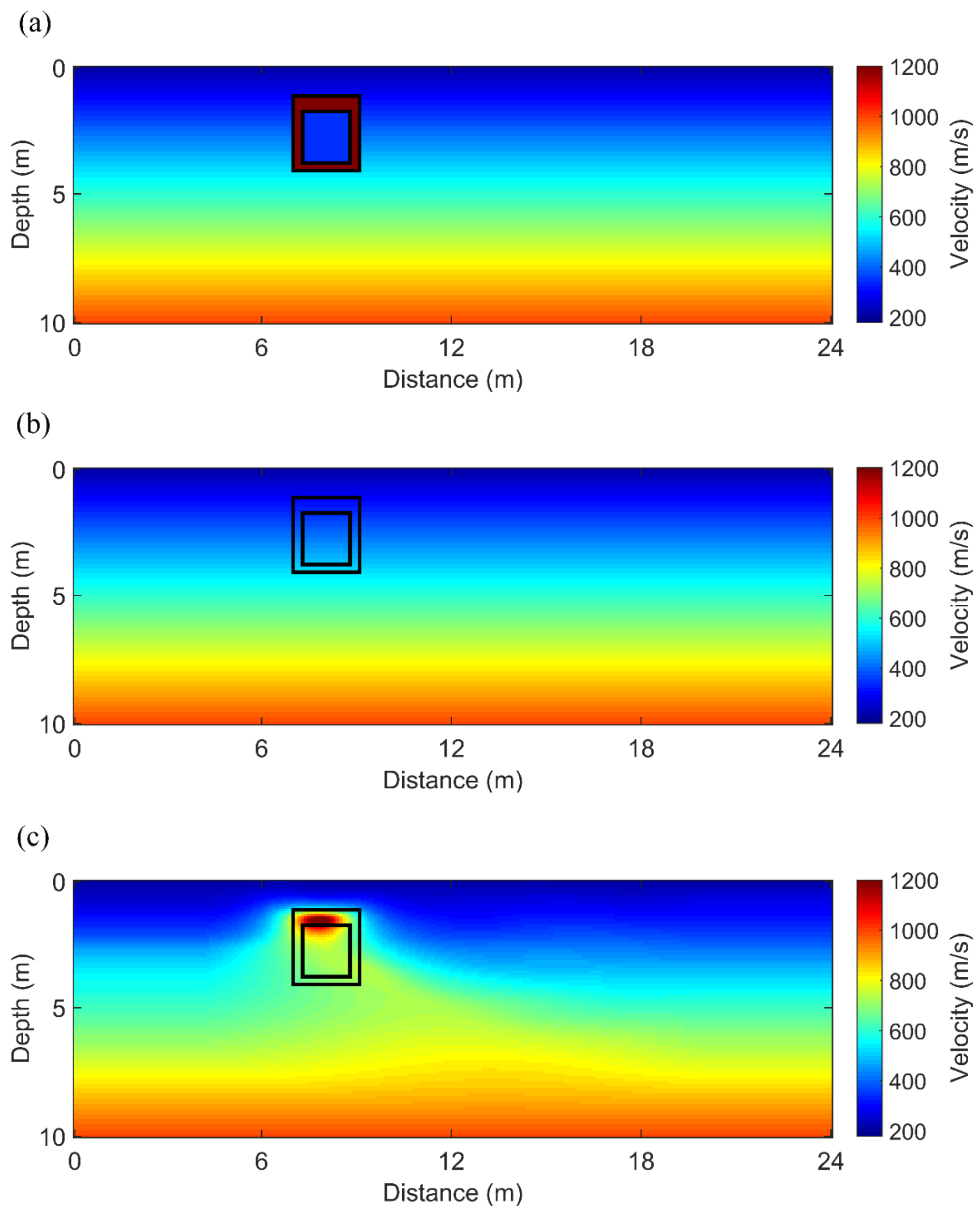

Fig. 1. (a) True model. (b) 1D linear gradient starting model. (c) Traveltime tomography models from synthetic data. The known concrete walls of the tunnel are indicated by black line.

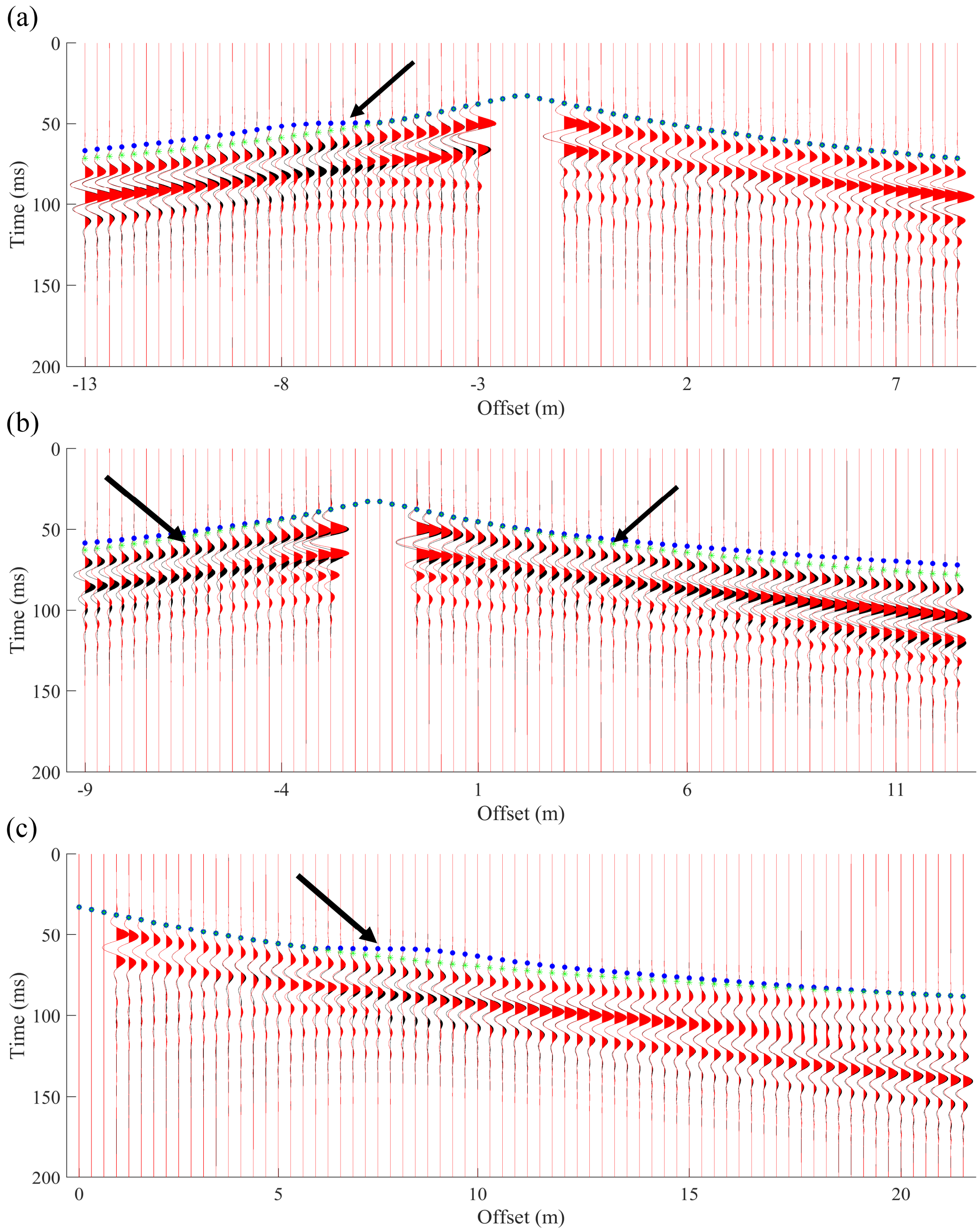

Fig. 2. Synthetic traveltime and waveform data. The blue dots and red waveforms represent traveltime and waveform calculated with true model. The green dots and black waveforms denote traveltime and waveform calculated with 1D linear gradient model. Near-offset waveform data are muted. The traveltime and waveform advances due to the tunnel walls are indicated by the black arrows. (a) Shot gather for X=0 m, (b) X=9 m, and (c) X=13 m.

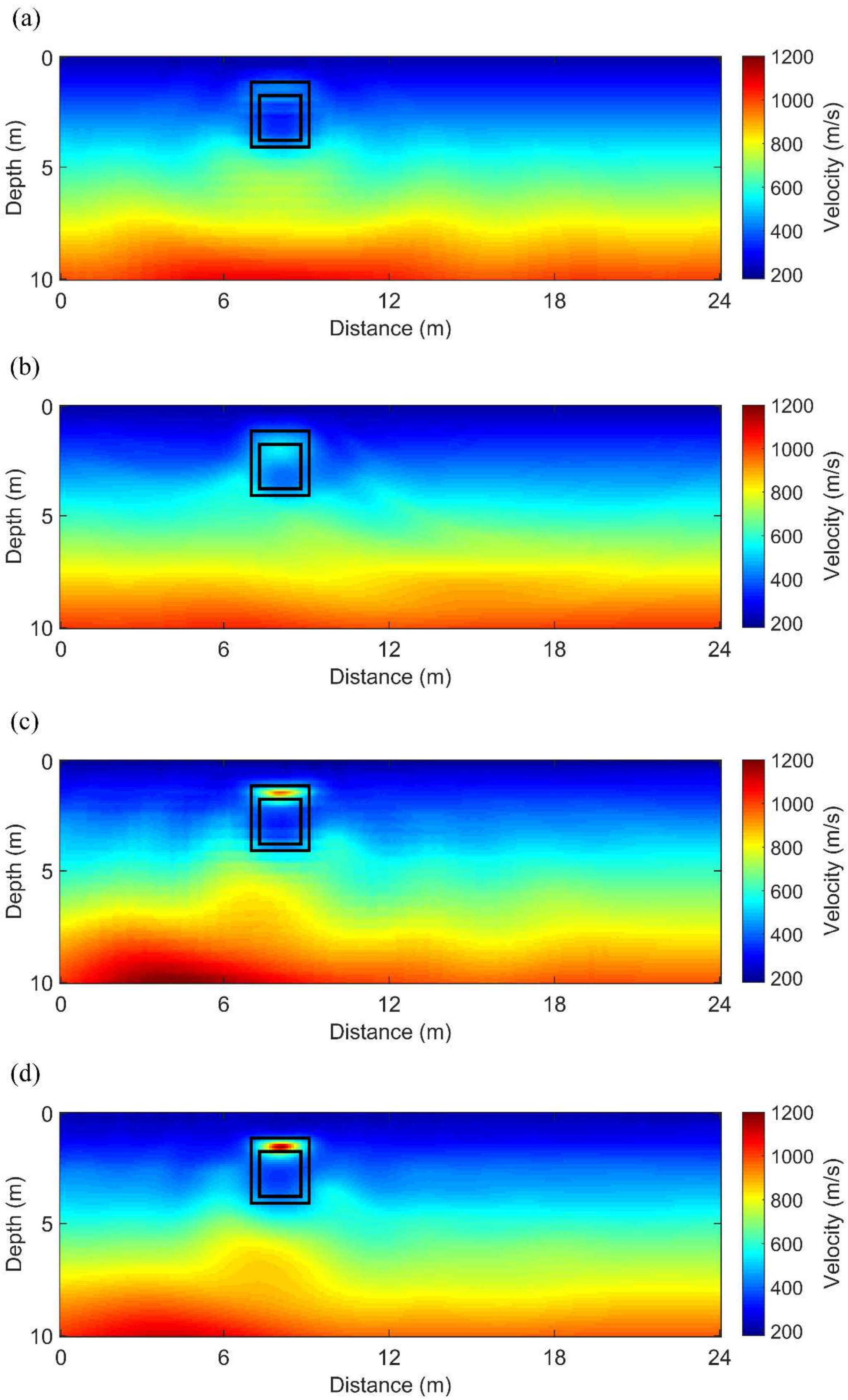

Fig. 3. FWI and the joint inversion models from synthetic data. (a) FWI model that uses the 1D model as the starting model. (b) The joint inversion model that uses the 1D model as the starting model. (c)

FWI model that uses the traveltime tomography model as the starting model. (d) The joint inversion model that uses the traveltime tomography model as the starting model.

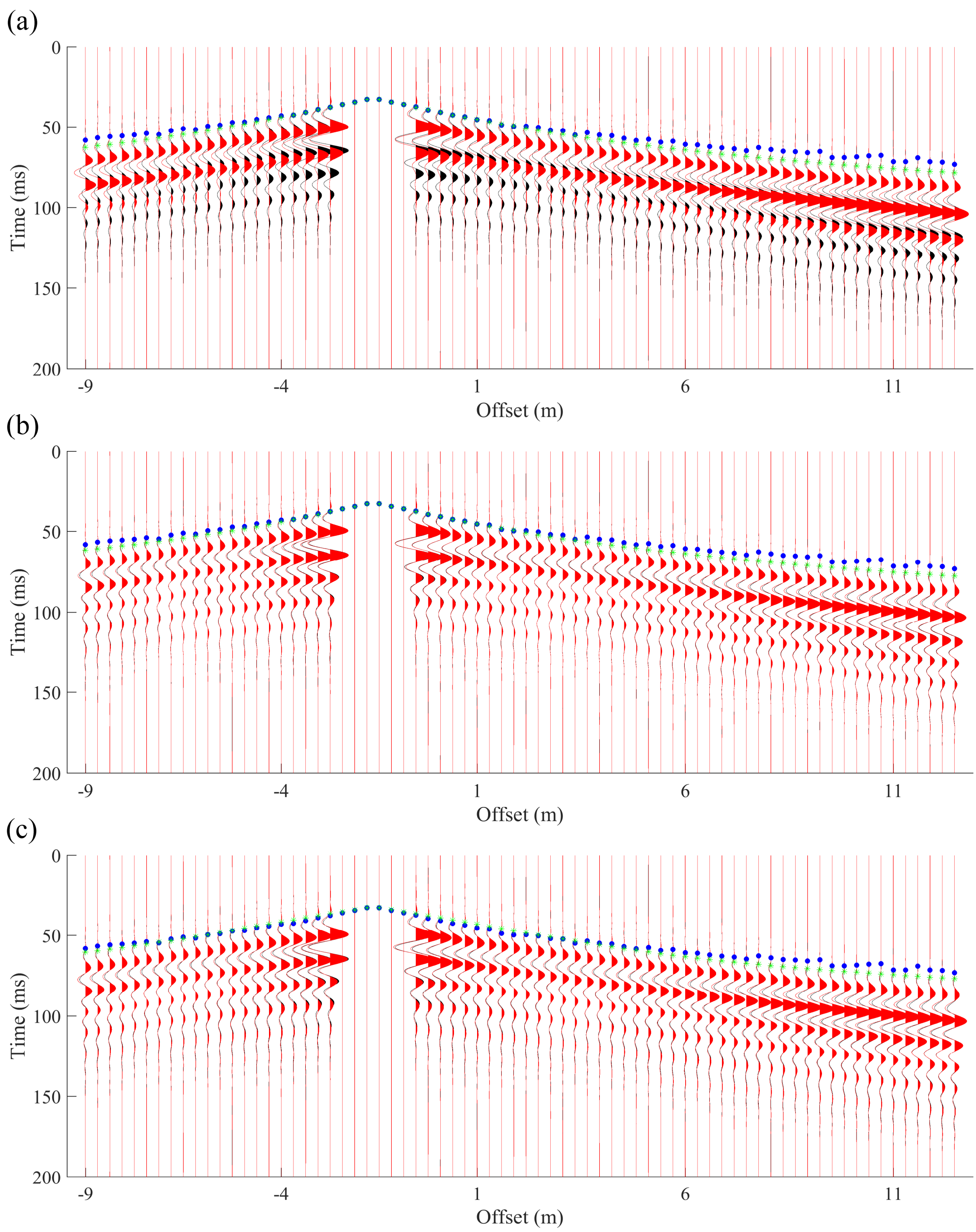

Fig. 4. Waveform overlay for shot gather at X=9 m using the 1D model as the starting model. (a) Initial waveform overlay. (b) FWI final waveform overlay. (c) Joint inversion final waveform overlay. Balck waveforms are observed data and red waveforms represent synthetic data. Blue dots denote observed traveltimes, green dots represent synthetic traveltimes.

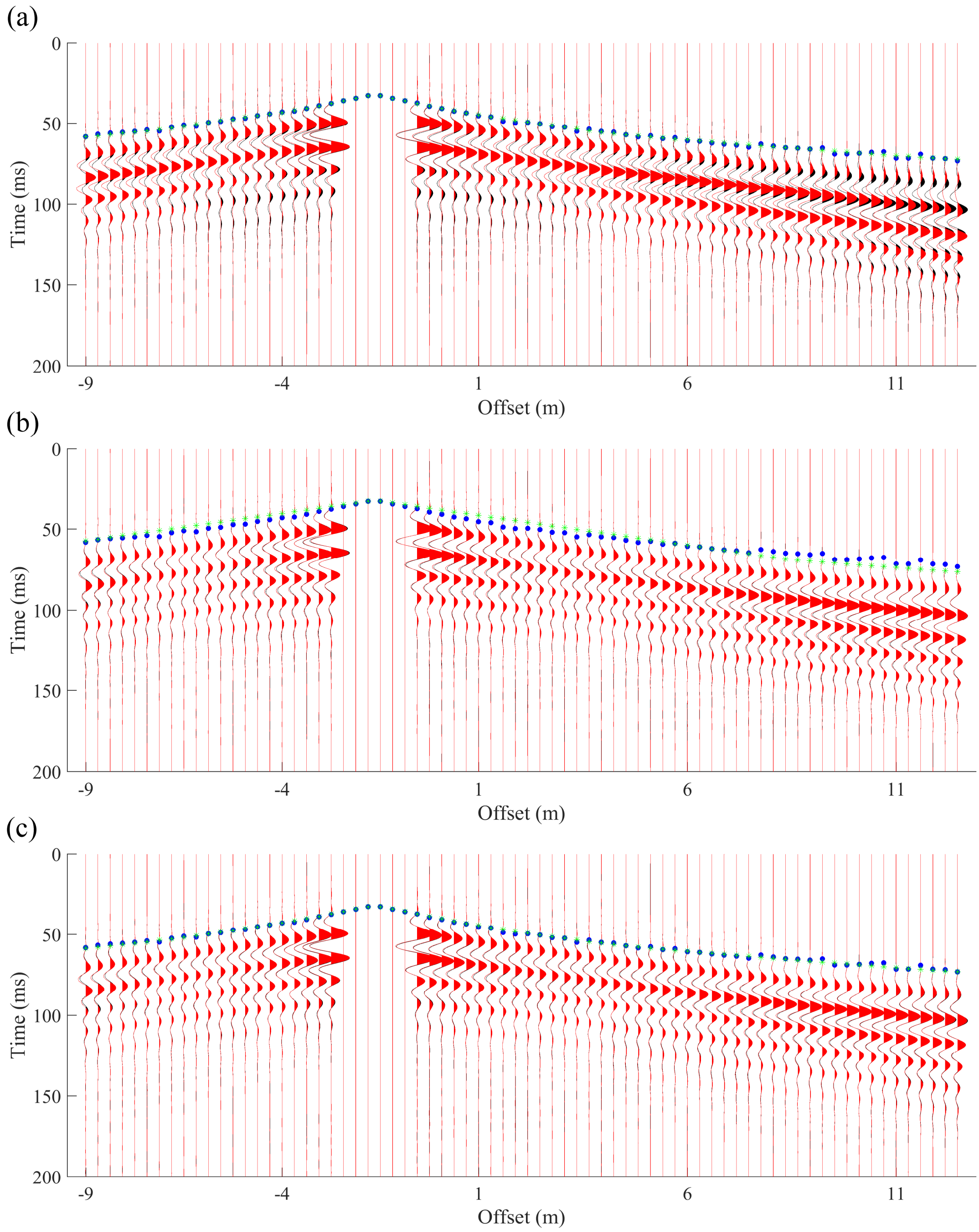

Fig. 5. Waveform overlay for shot gather at X=9 m using the traveltime tomography model as the starting model. (a) Initial waveform overlay. (b) FWI final waveform overlay. (c) Joint inversion final waveform overlay. Balck waveforms are observed data and red waveforms represent synthetic data. Blue dots denote observed traveltimes, green dots represent synthetic traveltimes.

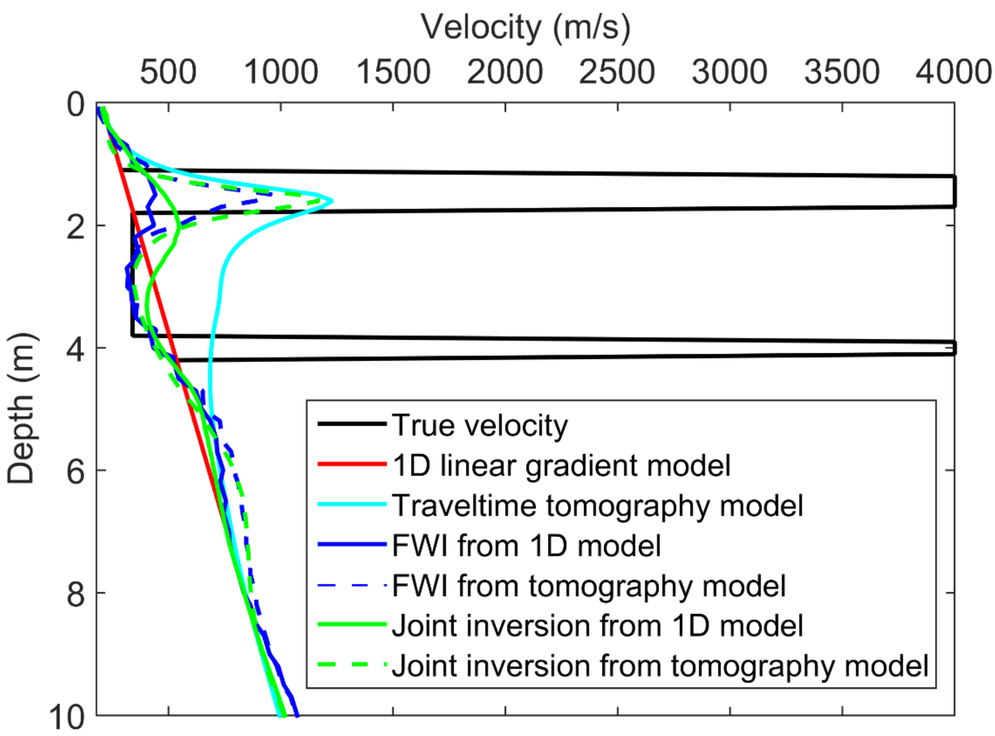

631

632 Fig. 6. 1D velocity profiles as labeled at X=8 m in the middle of the tunnel.

633

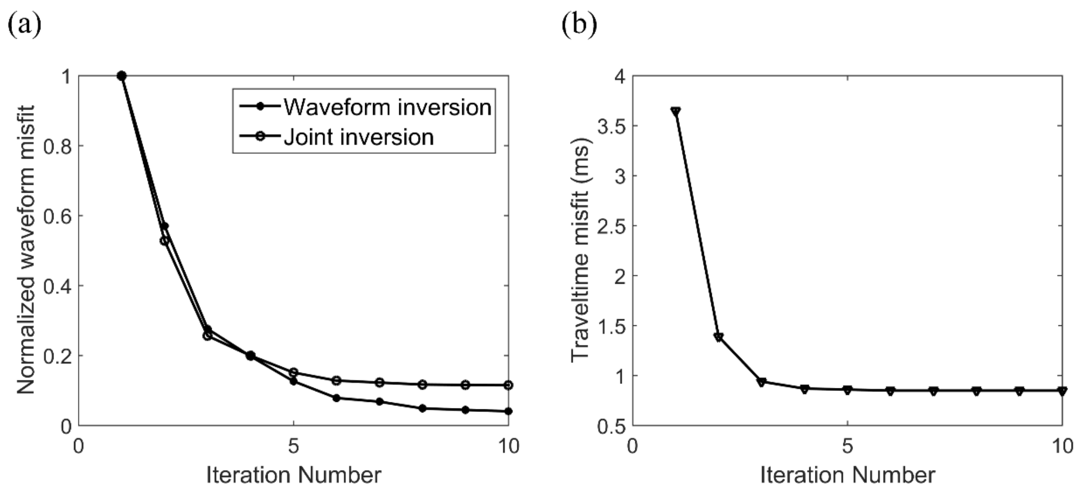

Fig. 7. Data misfit of the synthetic tests using a 1D starting model. (a) Normalized waveform misfit of FWI and the joint inversion. (b) Traveltime misfit of the joint inversion.

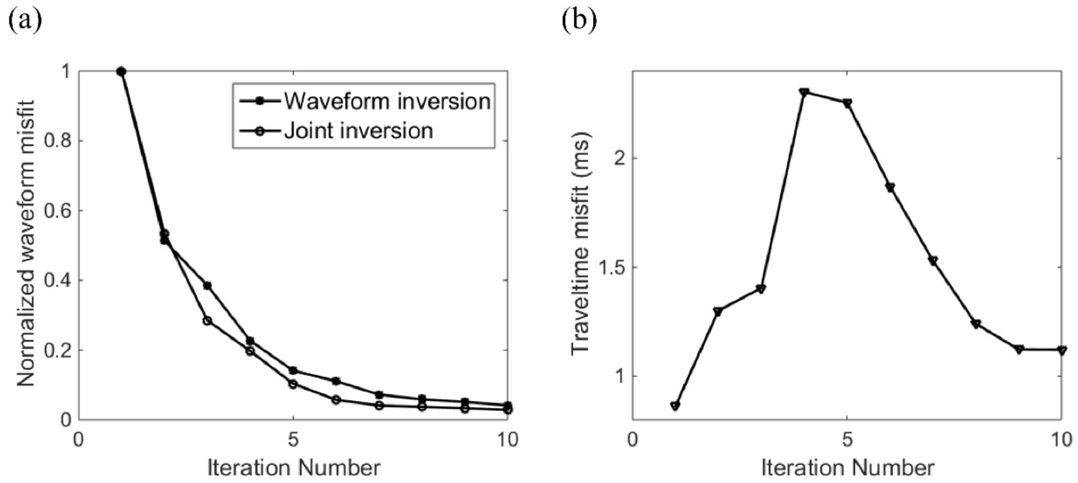

Fig. 8. Data misfit of the synthetic tests using the traveltime tomography model as the starting model. (a) Normalized waveform misfit of FWI and the joint inversion. (b) Traveltime misfit of the joint inversion.

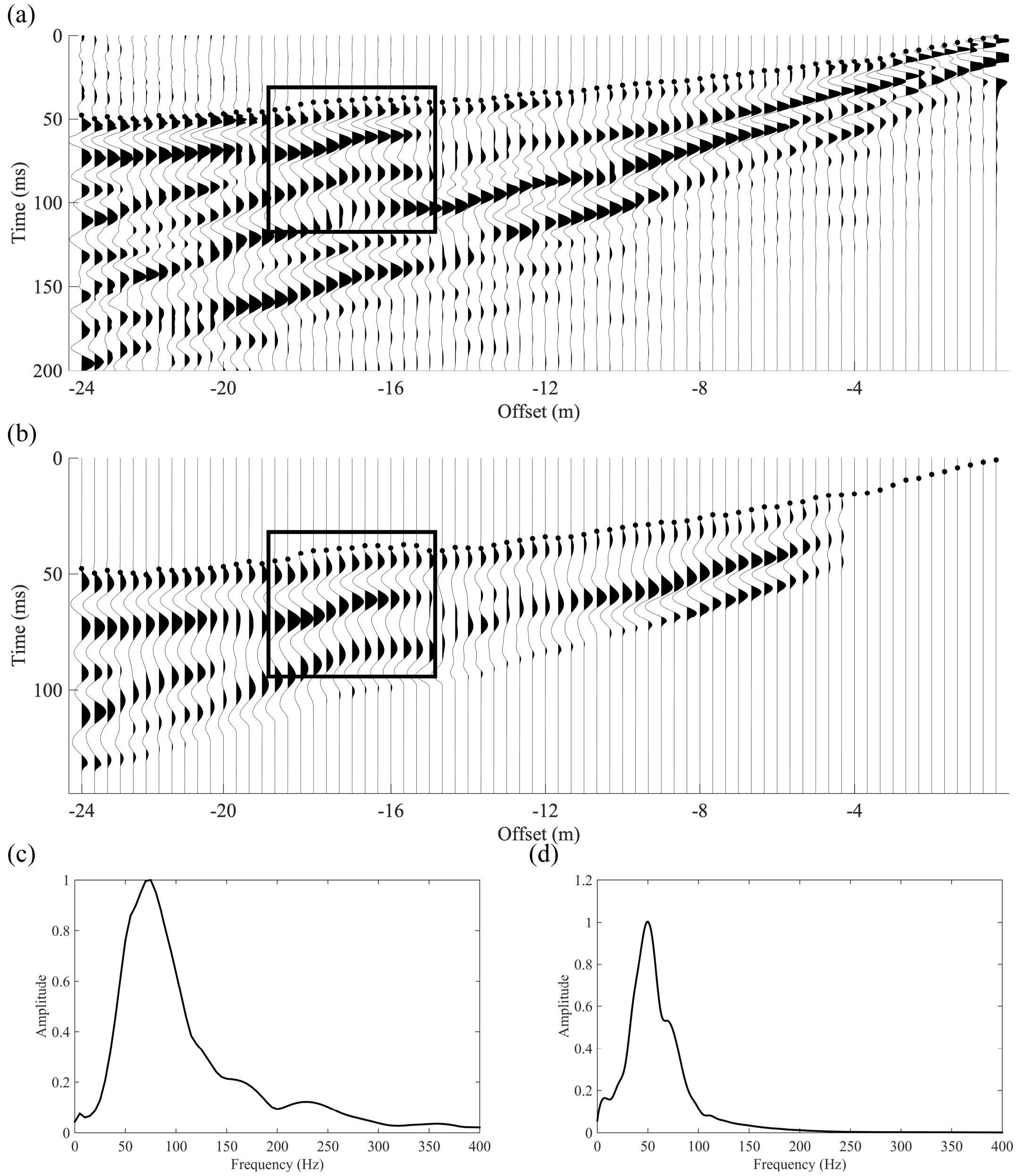

Fig. 9. (a) The raw shot gather of the real data at X=24 m. (b) The shot gather after preprocessing. (c) The average amplitude spectrum of the raw shot gather. (d) The average amplitude spectrum of the shot gather after preprocessing. Blue dots represent picked traveltimes. The waveform advances due to the tunnel walls are indicated by the black boxes.

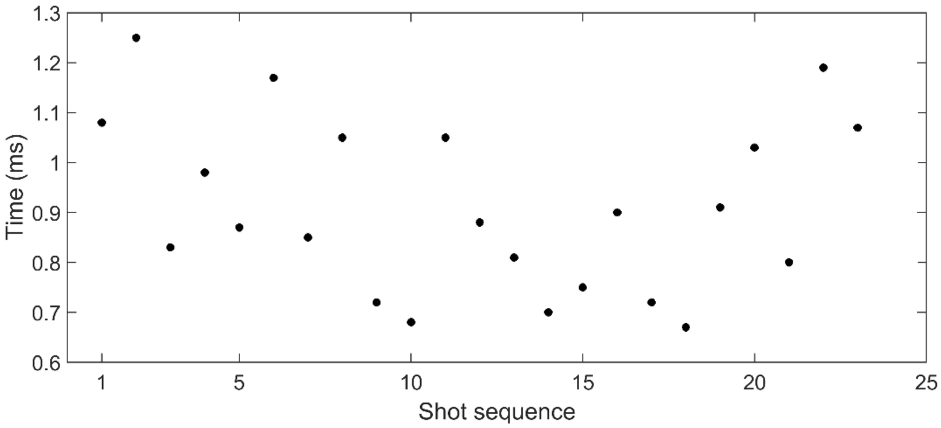

Fig. 10. The reciprocal error of the shots. The average reciprocal error is about 1 ms.

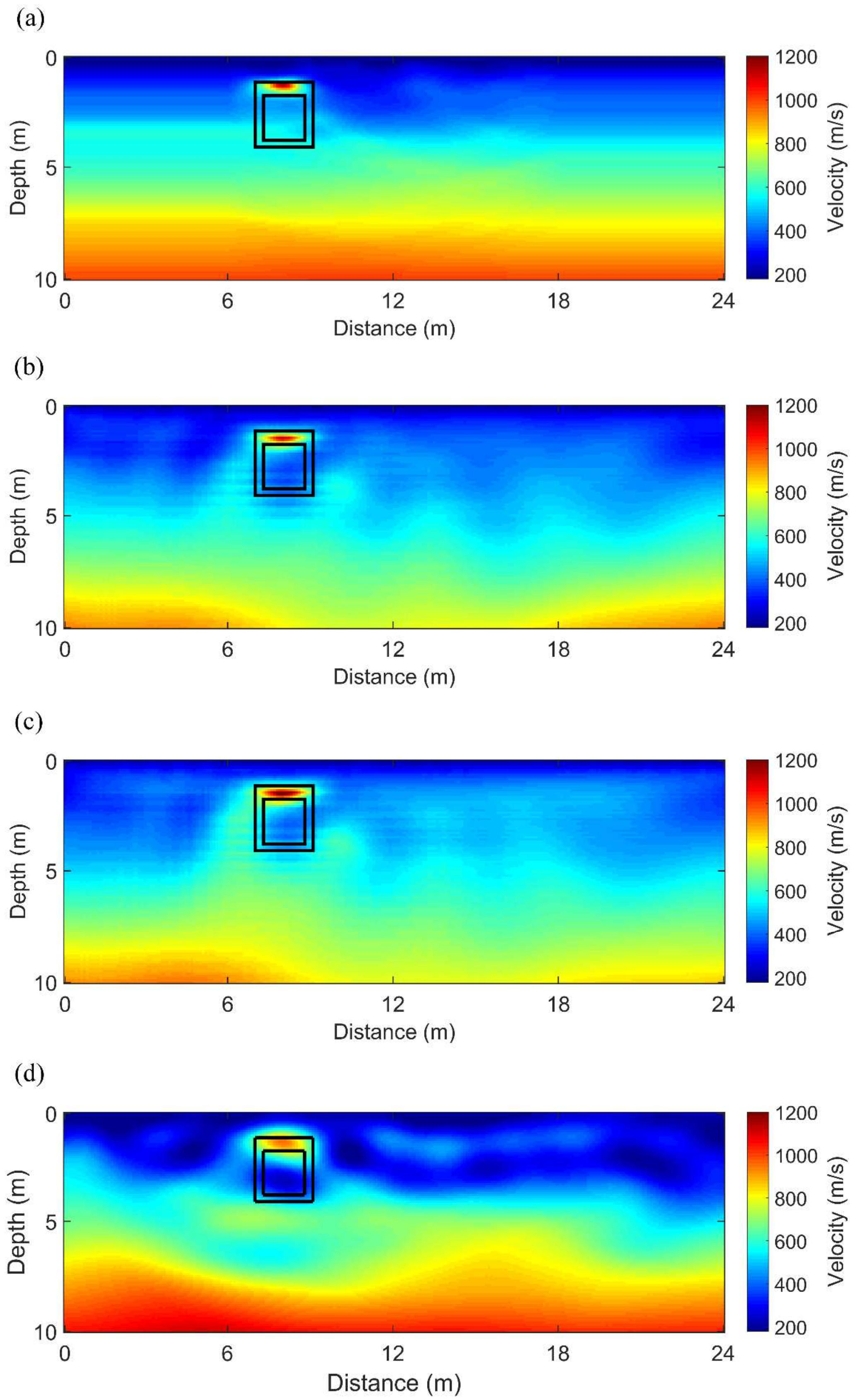

Fig. 11. Final models from real data. (a) Traveltime tomography model that uses the 1D model as the starting model. (b) FWI model that uses the traveltime tomography model as the starting model. (c)

The joint inversion model that uses the traveltime tomography model as the starting model. (d) The frequency domain FWI result from Chen et al. (2017).

658 .

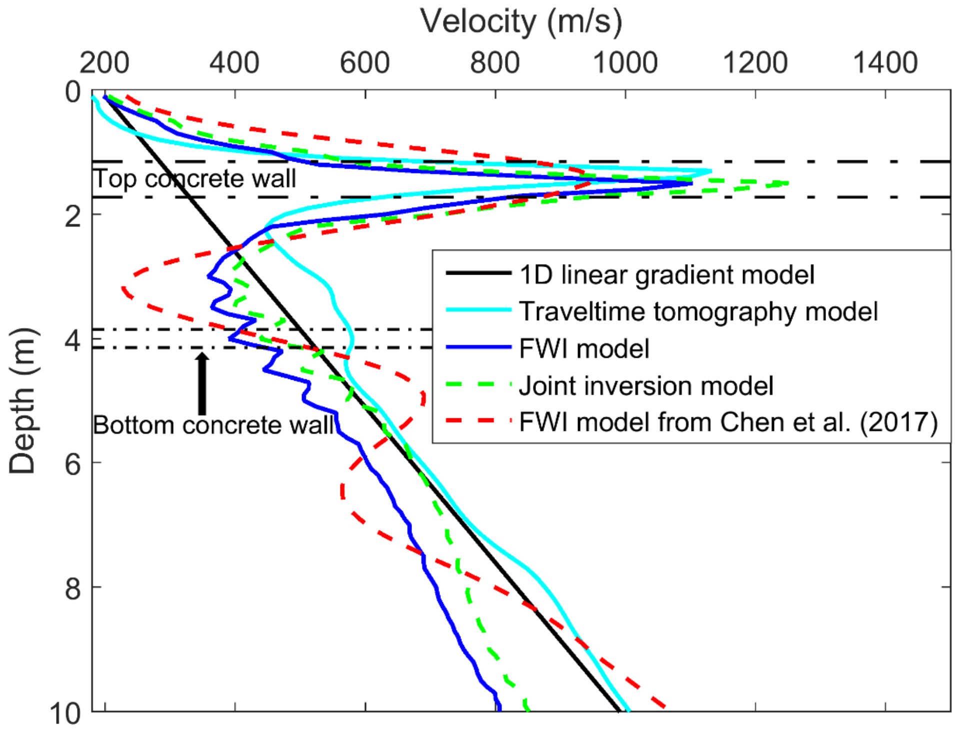

659

660 Fig. 12. 1D velocity profiles as labeled at X=8 m in the middle of the tunnel.

661

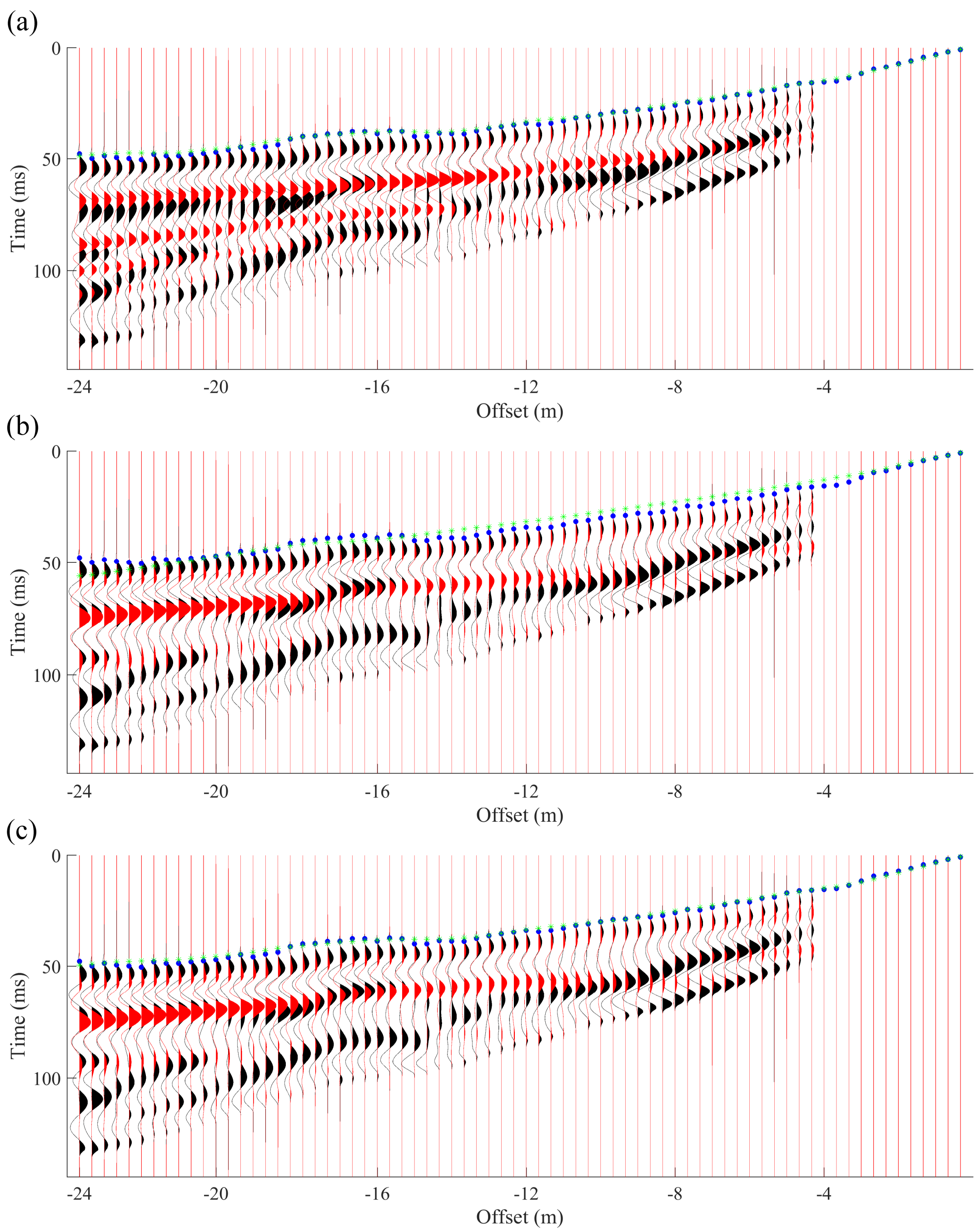

Fig. 13. Waveform overlays of a shot gather at X=24 m. (a) Waveform overlay between observed data (black) and synthetics (red) associated with traveltime tomography result. (b) Waveform overlay between observed data (black) and synthetics (red) associated with FWI result. (c) Waveform overlay between observed data (black) and synthetics (red) associated with the joint inversion result. Blue dots denote picked traveltimes, green dots represent synthetic traveltimes.

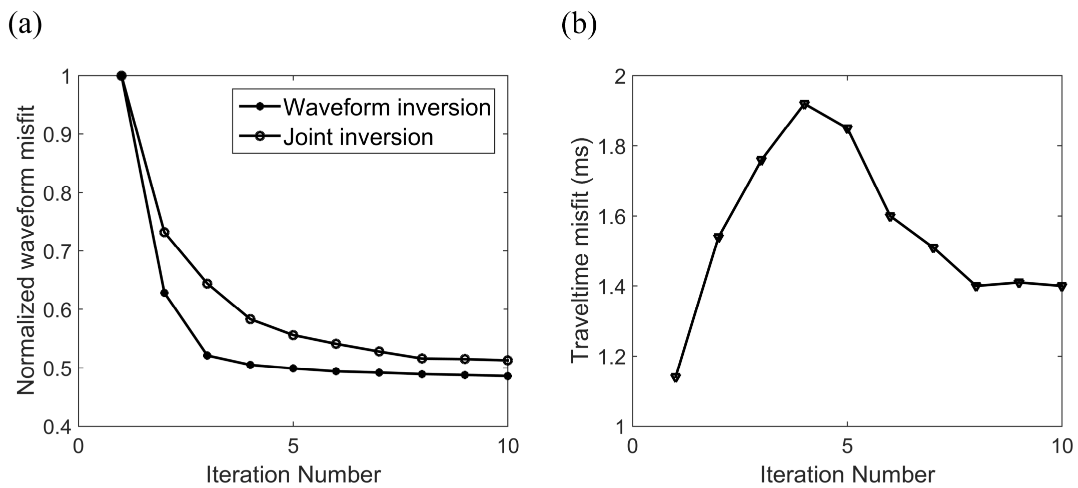

Fig. 14. Data misfit of the real data test (a) Normalized waveform misfit of FWI and the joint inversion. (b) Traveltime misfit of the joint inversion.

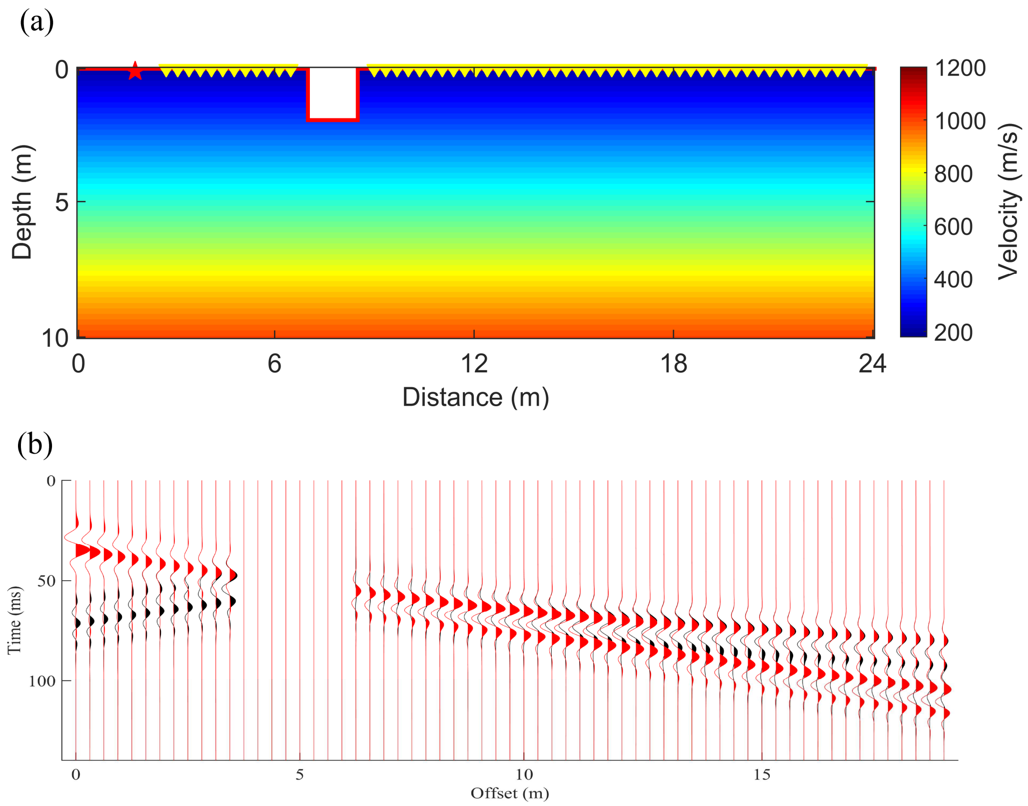

Fig. 15. (a) Benchmark model with an air-filled hole. The red star denotes shot, yellow triangles represent receivers. The red line is the surface topography. (b) Waveform overlay of the shot gather from Benchmark model (black) and model with 350 m/s replacement velocity (red).

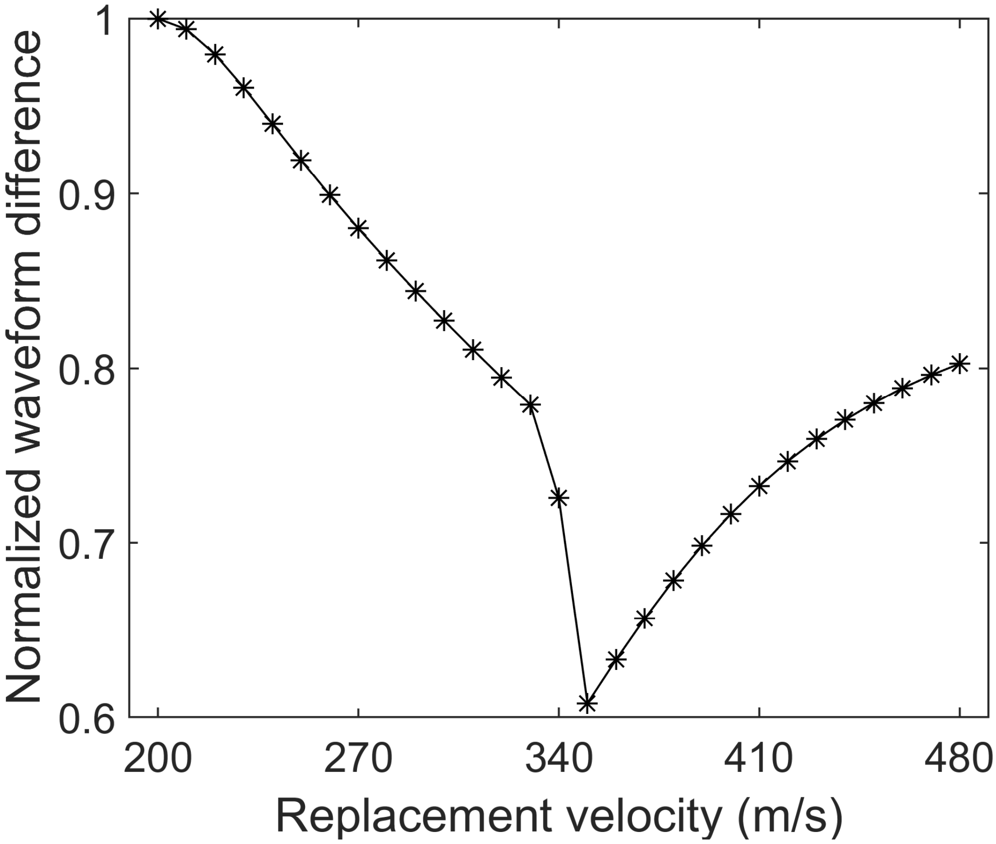

Fig. 16. Normalized waveform difference between velocity models filled with replacement velocity and benchmark model.